

Edge control in a computer controlled optical surfacing process using a heterocercal tool influence function

HAIXIANG HU,^{1,2,*} XIN ZHANG,¹ VIRGINIA FORD,³ XIAO LUO,¹ ERHUI QI,¹
XUEFENG ZENG,¹ AND XUEJUN ZHANG¹

¹Key Laboratory of Optical System Advanced Manufacturing Technology, Changchun Institute of Optics, Fine Mechanics and Physics, Chinese Academy of Sciences, Changchun, Jilin 130033, China

²University of Chinese Academy of Sciences, Beijing 100049, China

³Thirty Meter Telescope Observatory Corporation, Pasadena, California 91105, USA

*carrot723@gmail.com

Abstract: Edge effect is regarded as one of the most difficult technical issues in a computer controlled optical surfacing (CCOS) process. Traditional opticians have to even up the consequences of the two following cases. Operating CCOS in a large overhang condition affects the accuracy of material removal, while in a small overhang condition, it achieves a more accurate performance, but leaves a narrow rolled-up edge, which takes time and effort to remove. In order to control the edge residuals in the latter case, we present a new concept of the ‘heterocercal’ tool influence function (TIF). Generated from compound motion equipment, this type of TIF can ‘transfer’ the material removal from the inner place to the edge, meanwhile maintaining the high accuracy and efficiency of CCOS. We call it the ‘heterocercal’ TIF, because of the inspiration from the heterocercal tails of sharks, whose upper lobe provides most of the explosive power. The heterocercal TIF was theoretically analyzed, and physically realized in CCOS facilities. Experimental and simulation results showed good agreement. It enables significant control of the edge effect and convergence of entire surface errors in large tool-to-mirror size-ratio conditions. This improvement will largely help manufacturing efficiency in some extremely large optical system projects, like the tertiary mirror of the Thirty Meter Telescope.

© 2016 Optical Society of America

OCIS codes: (220.0220) Optical design and fabrication; (220.4610) Optical fabrication; (220.5450) Polishing.

References and links

1. V. Rupp, “The development of optical surfaces during the grinding process,” *Appl. Opt.* **4**(6), 743–748 (1965).
2. R. A. Jones, “Optimization of computer controlled polishing,” *Appl. Opt.* **16**(1), 218–224 (1977).
3. R. A. Jones, “Computer-controlled optical surfacing with orbital tool motion,” *Opt. Eng.* **25**(6), 256785 (1986).
4. J. Zimmerman, “Computer controlled optical surfacing for off-axis aspheric mirrors,” *Proc. SPIE* **1236**, 663–668 (1990).
5. N. Yaitskova and M. Troy, “Rolled edges and phasing of segmented telescopes,” *Appl. Opt.* **50**(4), 542–553 (2011).
6. D. Walker, G. Yu, H. Li, W. Messelink, R. Evans, and A. Beaucamp, “Edges in CNC polishing: from mirror-segments towards semiconductors, paper 1: edges on processing the global surface,” *Opt. Express* **20**(18), 19787–19798 (2012).
7. H. Li, D. Walker, G. Yu, A. Sayle, W. Messelink, R. Evans, and A. Beaucamp, “Edge control in CNC polishing, paper 2: simulation and validation of tool influence functions on edges,” *Opt. Express* **21**(1), 370–381 (2013).
8. H. Liu, F. Wu, Z. Zeng, B. Fan, and Y. Wan, “Edge effect modeling and experiments on active lap processing,” *Opt. Express* **22**(9), 10761–10774 (2014).
9. E. Luna-Aguilar, A. Cordero-Davila, J. Gonzalez, M. Nunez-Alfonso, V. Cabrera, C. I. Robledo-Sanchez, J. Cuautle-Cortez, and M. H. Pedrayes, “Edge effects with Preston equation,” *Proc. SPIE* **4840**, 598–603 (2003).
10. A. Cordero-Dávila, J. González-García, M. Pedrayes-López, L. A. Aguilar-Chiu, J. Cuautle-Cortés, and C. Robledo-Sánchez, “Edge effects with the Preston equation for a circular tool and workpiece,” *Appl. Opt.* **43**(6), 1250–1254 (2004).
11. H. S. Nam, G. C. Kim, H. S. Kim, H. G. Rhee, and Y. S. Ghim, “Modeling of edge tool influence functions for computer controlled optical surfacing process,” *Int. J. Adv. Manuf. Technol.* **83**(5-8), 911–917 (2016).

12. D. W. Kim, W. H. Park, S. W. Kim, and J. H. Burge, "Parametric modeling of edge effects for polishing tool influence functions," *Opt. Express* **17**(7), 5656–5665 (2009).
13. H. Hu, E. Qi, and G. Cole, "Research on sub-surface damage and its stress deformation in the process of large aperture and high diameter-to-thickness ratio TMT M3MP," *Proc. SPIE* **9682**, 968244 (to be published).
14. H. Hu, X. Luo, and H. Xin, "Layout optimization of equal-force supports for ultra large optical fabrication," *Acta Opt. Sin.* **34**(4), 0422003 (2014).
15. V. G. Ford, "Tertiary mirror surface figure specification," Thirty Meter Telescope Observatory Corporation document, TMT.OPT.SPE.12.001.DRF02, 2014, available at <http://www.tmt.org/sites/default/files/documents/application/pdf/tmt%20-%20tertiary%20mirror%20surface%20figure%20specifications%2020121023.pdf>.
16. H. Hu, Y. Dai, X. Peng, and J. Wang, "Research on reducing the edge effect in magnetorheological finishing," *Appl. Opt.* **50**(9), 1220–1226 (2011).
17. P. Guo, H. Fang, and J. Yu, "Edge effect in fluid jet polishing," *Appl. Opt.* **45**(26), 6729–6735 (2006).
18. J. González-García, A. Cordero-Dávila, I. Leal-Cabrera, C. I. Robledo-Sánchez, and A. Santiago-Alvarado, "Calculating petal tools by using genetic algorithms," *Appl. Opt.* **45**(24), 6126–6136 (2006).
19. Wikipedia article, "Fish fin," https://en.wikipedia.org/wiki/Fish_fin#AnchCaudal.
20. F. Preston, "The theory and design of plate glass polishing machines," *J. Soc. Glass Technol.* **9**, 214–256 (1927).
21. H. Hu and X. Zhang are preparing a manuscript to be called "Time-varying heterocercal tool and its application in large optical primary mirror with a central hole."
22. Delta Tau China technical support, "IMAC 400 details," <http://www.deltatau-china.com/html/xt/2449.html>.
23. L. Li, L. Zheng, W. Deng, X. Wang, X. Wang, B. Zhang, Y. Bai, H. Hu, and X. Zhang, "Optimized dwell time algorithm in magnetorheological finishing," *Int. J. Adv. Manuf. Technol.* **81**(5-8), 833–841 (2015).

1. Introduction

Computer controlled optical surfacing (CCOS) processes have been developed and used since 1963 [1–4]. In a CCOS process, the amount of the removed material is determined by the tool influence function (TIF) and the dwell time. However, when the tool moves near the border of the workpiece, it causes a nonuniformity in the material removal and the edge effect [5]. Traditional opticians need to balance working parameters for various kinds of tools and workpieces to ensure a good clear aperture. Based on previous research results [6–11], the edge effect includes two parts:

1. Turned-up edges (TUEs). To avoid tool tipping at the edge, the computer controls the tool pin inside the workpiece by maintaining a certain distance from the edge. When the tool does not move far enough over the workpiece edge, material removal near the edge is less than that in the inner region, leaving the edges rolled up.
2. Turned-down edges (TDEs). As the tool partly hangs over the edge, the trend to tip produces a torque, and makes the pressure distribution relatively larger near the edge. TIF near the edge is not as expected. In a large overhang situation, the tool will cause the edges to be rolled down.

It would be advantageous to know exactly the effect of tool overhang. Some correction models can be used to predict the TIF at the edge. In 1986, Jones suggested a linear model for the pressure distribution [3]. In 2004, Luna-Aguilar developed the skin model for the non-linear approach [9]. In 2016, Nam reported the modified FEA model for accurate prediction of the pressure distribution [11]. In 2009, Kim established a parametric model of edge TIFs, which is able to describe edge TIFs in parametric polynomial ways [12]. The overhang ratio S is defined as the ratio of the overhang distance to the tool width in the overhang direction. The reported experiments indicated that increasing overhang ratio enlarges the fitting residual error of the removal profile. In other words, less overhang creates higher accuracy.

On the other hand, some low-stiffness, non-round workpieces or those with perimeter corners probably do not fit the edge model perfectly. Take the tertiary mirror of the Thirty Meter Telescope (TMT) for an instance, it is designed to be the world largest optical flat as part of the Giant Steerable Science Mirror (GSSM) system. The mirror is elliptical in shape, $3.5\text{m} \times 2.5\text{m}$ across, and only 100mm thick, with diameter-to-thickness ratio of 36 [13]. During fabrication, a system of 144 hydrostatic units has been designed to support the 'soft'

mirror, resulting in inevitable surface deformations and pressure changes caused by self-weight deflection, the tool pressure, and the supports. Additionally, as shown in Fig. 1, when using the same tool overhang distance, the overhang area changes around the mirror, which changes the loading on the support points. This increases the difficulty of knowing exactly the pressure distribution to use in the analytic model, and makes the boundary conditions more critical for the finite element analysis (FEA) modeling. It means that the overhang distance of the tool must be shortened to reduce this effect.

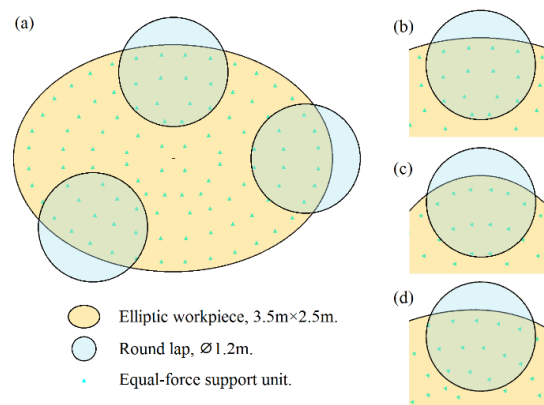






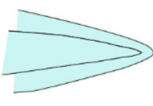
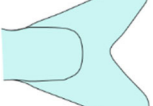
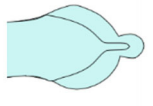
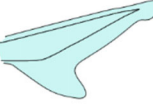
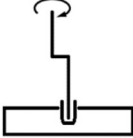
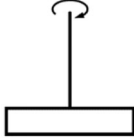

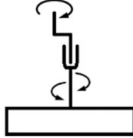
Fig. 1. Overhanging situation of 1.2m lap on the elliptic TMT M3 mirror (3.5m × 2.5m, supported by 144-point system in fabrication status [14]). a) 3 typical positions with the same overhang distance. b) Less overhang area in minor axis. c) More overhang area in major axis. d) Asymmetric overhang area in other directions.

A set of relatively small sizes of tools could be used to avoid significant overhang; however, due to the lack of efficiency, that is not a good choice for large mirrors. Also, small tools are more likely to add high spatial frequency surface error which is very restricted in GSSM specification [15] in the form of slope-RMS.

In other sub-aperture polishing techniques, some methods were applied to reduce the edge effect. In magnetorheological finishing (MRF) process, a small removal function was adopted and compensated with modeling at the edge of the workpiece [16]. In fluid jet polishing (FJP), FEA model was used to simulate the distributions of both the velocity and the pressure of the slurry jets, in order to obtain the precise TIF at the edge [17].

The focus of our work is to control the TUEs using relatively large tools, and at the same time, introduce the least overhang and uncertainty. The tool is expected to be round in shape, so that high symmetry ensures expansibility and applicability. A round polishing tool library normally includes the orbital tool, the spin tool, the solid tool, and the petal tool [18], etc. Table 1 shows edge removal profiles of different tools. They are similar to some types of fishes' arch caudal in appearance. Inspired by the heterocercal tails of sharks, an idea of a possible new type TIF is also given in the 4th column.

Table 1. TIF types of round tools and the edge TIF profiles accordingly.

TIF type	Gaussian-like	V-shape	Centralized	Skewed shape
Edge removal profile [5]				
Typical arch caudal of fishes ^a				
Possible mechanism				

^aFrom left to right, there are protocercal, homocercal, diphycercal, heterocercal [19].

In comparison, the skewed TIF, or ‘heterocercal’ TIF, potentially has better performance in controlling TUEs, because the peak of the removal is close to the edge. In this paper, we provide the ‘heterocercal’ TIF type where a combination of continuous orbital stroke and swing spin is put into use for the first time. The orbital stroke produces a uniform relative speed between the tool and the workpiece. The swing stroke transfers the removal distribution from the inner edge to the tool to the outer edge.

With the guidance of this concept, we present the possibility of the heterocercal TIFs based on Preston’s equation (linear model) [20]. The working parameters of the concept are optimized in Section 2. In Section 3, the mechanical structure is developed, and the high precision of the control system is achieved. Utilizing this facility, what we called ‘H-Z trimmer’, the experimental demonstration of this TIF and simulative convergence instance are summarized in Sections 4 and 5, respectively.

2. Theory of the heterocercal TIF

The TIF can be calculated based on the equation of material removal, Δz , which is known as the Preston’s equation [20],

$$\Delta z(x, y) = \kappa \cdot p(x, y) \cdot v(x, y) \Delta t. \quad (1)$$

Here Δz is the integrated material removal from the workpiece surface, κ is the Preston coefficient, p is the pressure at the tool-work piece contact position, v is the magnitude of relative speed between the tool and workpiece surface and Δt is the dwell time. The equation assumes that the integrated material removal, Δz , depends on p , v , and Δt linearly.

2.1 Concept

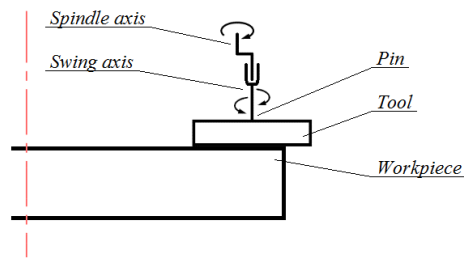


Fig. 2. Heterocercal concept.

During the Orbital motion, the tool strokes around the spindle axis, resulting in a uniform distribution of the velocity magnitude, which is given by,

$$v(x, y, t) = s \cdot \omega_a, \text{ assuming } \omega_a > 0. \quad (2)$$

Here, s (a constant) is the distance from the center pin of the tool to the spindle axis, or the radius of the stroke, and ω_a is the revolution speed. The heterocercal concept is to rearrange the velocity field with a swing motion, as shown in Fig. 2 and Fig. 3.

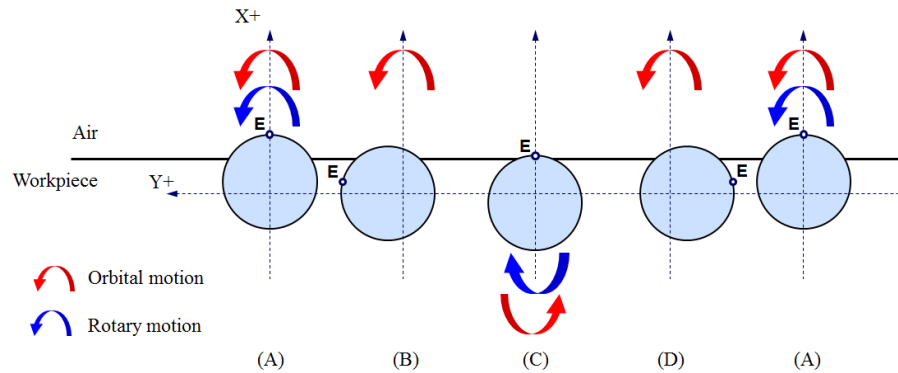


Fig. 3. Schematic diagram of the 'heterocercal' motion strategy.

When the tool travels to status A (most overhang), the Orbital motion provides a uniform velocity field in the + Y direction. An additional counter-clockwise spin motion, Rotary motion, will rearrange the velocity field, and make the instantaneous rotary center move to the negative side of the X-axis. As a result, the instantaneous tool velocity near the mirror edge is larger, and the velocity towards the inside of the mirror is smaller. So the material removal towards the mirror edge is expected to be larger than toward the mirror center, creating a better edge. Likewise, when the tool travels to status C (least overhang), the uniform velocity field (along -Y) of Orbital motion plus a clockwise Rotary motion creates the same removal effect.

The rearranged velocity distribution is expected to be symmetric along the pin-to-spindle line. It means that, in status B and D, the additional spin motion will not rearrange the velocity field towards the edge. Hence in a stroke period, i.e. A-B-C-D-A, spin motion also passes through a period like (+)-(0)-(-)-(0)-(+). For the conveniences of analysis and, more important, the system control, the swing spin motion is designed in cosine mode, which can be expressed as:

$$\omega_b = k\omega_a \cos\left(2\pi \frac{t}{T}\right), k > 0, T = \frac{2\pi}{\omega_a}. \quad (3)$$

Here, k (not κ) is a constant magnitude ratio of angular speed, or the heterocercal coefficient; ω_b is the angular speed of the spin motion; and T is the entire period of one stroke.

2.2 Velocity field and material removal distribution

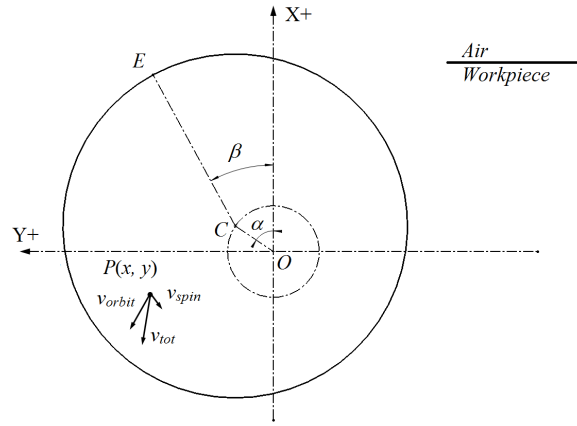


Fig. 4. Schematic diagram of velocity field of orbital and spin tool motion combination.

Figure 4 shows a schematic diagram of two velocity fields generated from orbital motion \mathbf{v}_{orbit} and spin motion \mathbf{v}_{spin} . Here α is orbital angle, and β is rotary angle. As E is a fixed point on the tool, Eq. (3) is rewritten in angular parameters,

$$\omega_b = k\omega_a \cos \alpha, \text{ with } \omega_a = d\alpha/dt, \omega_b = d\beta/dt. \quad (4)$$

The instantaneous tool speed experienced by the $P(x, y)$ coordinate on the workpiece surface at any given time t can be expressed as,

$$\vec{v} = \vec{v}_{orbit} + \vec{v}_{spin} = |OC|\omega_a e^{i(\alpha+\pi/2)} + |CP|\omega_b e^{i(\beta+\angle ECP+\pi/2)}. \quad (5)$$

$$v(x, y) = \sqrt{\omega_b^2 (x^2 + y^2) + 2(\omega_a - \omega_b)\omega_b s(x \cos \alpha + y \sin \alpha) + (\omega_a - \omega_b)^2 s^2}. \quad (6)$$

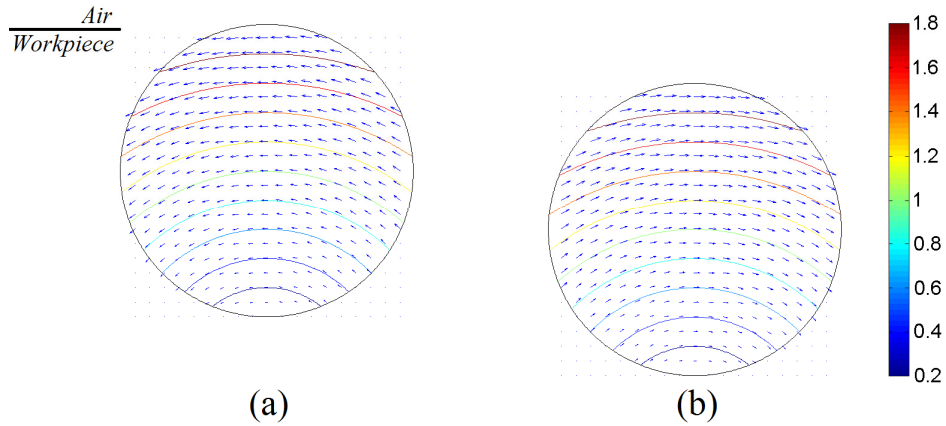


Fig. 5. Instantaneous tool speed distribution in vector and contour map over the time period. a) Most overhang, status A ($t = 0$). b) Least overhang, status C ($t = T/2$).

Figure 5 is a graphical representation of Eq. (6), which is an axial-displaced V-shape distribution.

The pressure exerted onto the workpiece is uniform, similar to simple orbital tools or spin tools. The pressure distribution can be expressed by the circle function in Eq. (7).

$$p(x, y) = p_0 \cdot \text{circ}\left(\frac{x - s \cos \alpha}{r_0}, \frac{y - s \sin \alpha}{r_0}\right). \quad (7)$$

Here, r_0 stands for the radius of the tool. The function is defined by $\text{circ}(x, y) = 1$, when $0 \leq x^2 + y^2 \leq 1$, and is 0 otherwise. Base on Preston equation, after one stroke, the material removal distribution is given by,

$$\Delta z = \int_{t=t_0}^{t_0+T} \kappa \cdot p(x, y) \cdot v(x, y) dt = \int_{\alpha=0}^{2\pi} \kappa \cdot p(x, y) \cdot v(x, y) \frac{d\alpha}{\omega_a}. \quad (8)$$

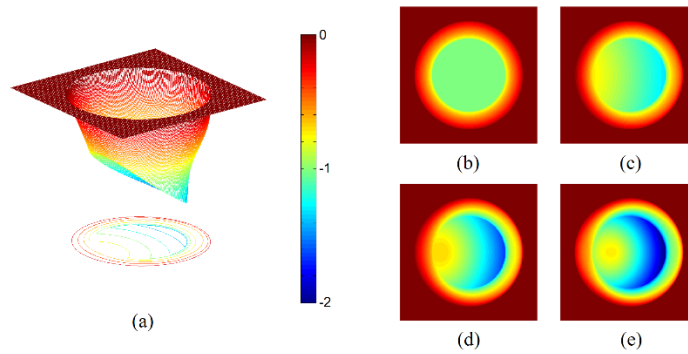


Fig. 6. Simulative heterocercal TIFs in the normalized color axis. a) $k = 0.25$. b) $k = 0.00$ (Orbital mode). c) $k = 0.15$. d) $k = 0.30$. e) $k = 0.45$.

Figure 6 gives a graphic representation of Eq. (8). In the numerical simulation, the tool diameter $D = 1.2\text{m}$, the orbital radius $s = 120\text{mm}$. As the heterocercal ratio k varies, the material removal distribution shows different extents of slant. Besides, in Fig. 6(d), the shape of TIF starts to change, and in Fig. 6(e), is distorted in the central part (V-shape). It calls for some further optimization design in the working parameters.

2.3 Parametric optimization design

This type of tool should be optimized for two goals. One is to enlarge the slope of TIF, thus remove more material near the edge of workpiece. The other is to avoid a strong V-shape in the center part of TIF, making the removal distribution smooth enough for better convergence. Based on the above simulation, increasing coefficient k may help the slope, but hurt the convergence ability.

In one stroke, the tool constantly touches the central part of the spot. According to Fig. 6(d), the deformation of TIF also occurs in this area, where $p = p_0$. With the help of above mentioned velocity field, the material removal in the central part is given by,

$$\Delta z = \kappa \cdot p_0 \int_{\alpha=0}^{2\pi} v(x, y, t) \frac{d\alpha}{\omega_a}. \quad (9)$$

In Fig. 7, four profiles of the central TIFs are plotted out in X direction (where $y = 0$), according to Eq. (9), which is also in the axial-displaced V-shape. Here, the horizontal axis is labeled x/s , where x and s represent the distance and the constant stroke radius respectively.

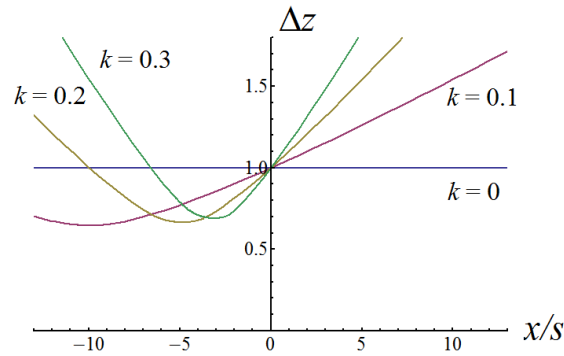


Fig. 7. Normalized material removal profile in X direction.

As shown in Fig. 7, the profiles cluster shows a set of asymptotic minimum points, when $k \neq 0$. At the minimum value, x coordinate is around -10 , -5 , and -3 , when $k = 0.1$, 0.2 , and 0.3 . After a set of reduction [21] from Eq. (9), the minimum point of the normalized profile has an approximate solution in accord with the above phenomenon, where,

$$\Delta z_{\min} \approx \frac{2}{\pi}, \text{ when } \frac{x}{s} \approx -\frac{1}{k}. \quad (10)$$

Equation (10) indicates that, to avoid any distortion, the size of the central part should be restrained by,

$$D - 2s \leq \frac{2s}{k}. \quad (11)$$

Hence, we get an optimized parameter k by,

$$k = \frac{2s}{D - 2s} \approx \frac{2s}{D}. \quad (12)$$

Here D stands for the tool diameter, and s for orbital radius as previously mentioned.

2.4 Improvement in TUEs control

In this section, the edge TIF [5] is to be analyzed, in order to chart the improvement in TUE control quantitatively and effectively. The edge TIF, or the edge profile can be generally expressed by,

$$\Delta z = \frac{1}{D + 2s} \int_{y=-D/2-s}^{D/2+s} \int_{\alpha=0}^{2\pi} \kappa \cdot p(x, y) \cdot v(x, y) \frac{d\alpha}{\omega_a}. \quad (13)$$

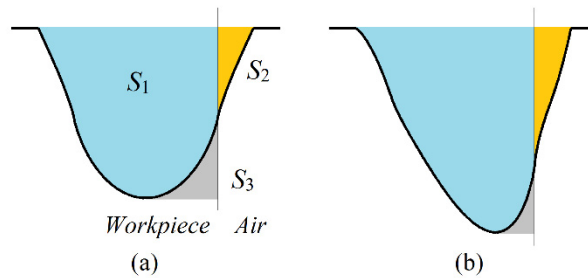


Fig. 8. Scheme of the material removal profile of the edge TIFs. a) Orbital tool. b) Heterocercal tool.

The path of the integration is along the straight border of the workpiece, i.e. Y direction. Figure 8 shows the different material removal profiles of the edge TIFs in orbital mode and heterocercal mode from Eq. (13). With the same edge overhang ratio, the heterocercal mode produces the smaller TUE. For a quantitative comparison, the TUE residual rate (TUR) is defined by,

$$TUR = \frac{S_3}{S_1} \times 100\%. \quad (14)$$

Here $S_1 + S_2$ stands for the nominal material removal, S_1 for the effective removal, S_2 for unrealized removal that would occur in the overhang region, and S_3 for the TUE residuals. By definition, this rate is determined by the distribution of edge TIF and overhang ratio, if without any modification on pressure distribution. Lower TUR helps the efficiency of the material removal of the edge, and will cause less edge effects.

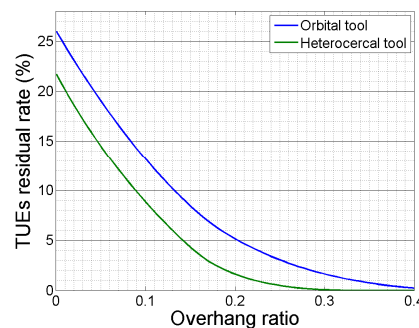


Fig. 9. TUE residuals of orbital tool and heterocercal tool.

Figure 9 shows the TUE features of orbital tools and heterocercal tools. Here $D = 1.2\text{m}$, $s = 120\text{mm}$, $k = 0.25$. It reveals that if we plan to restrain the TUR under 3%, the overhang ratio should be larger than 0.25 in orbital mode, but only 0.17 in heterocercal mode. From another point of view, when working with the same overhang ratio 0.17, the orbital tool will leave 7% TUEs, which is 2.3 times larger than the heterocercal tool. This indicates that the heterocercal tool is expected to bring significant improvement in TUE control and potentially is capable of more accurate surface error convergence.

3. Mechanical realization

Through the above analysis, the heterocercal TIFs, compared to the Gaussian-like ones, have the advantage that the peak of the TIF can be precisely controlled and shifted. To physically achieve this, high accuracy must be used in the realization of the mechanical structure and the control system. Here, a prototype was fabricated to test the theory.

3.1 Structure

In order to drive the tool with the desired motion combination, a compound motion equipment has been designed. It attaches to the present machine's main spindle to produce a compound motion. The size of the driven tool is designed as $\varnothing 80\sim 400$ in mm.

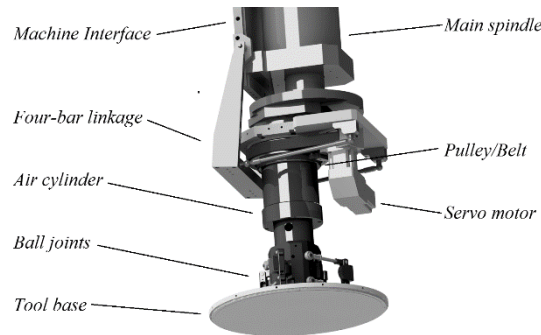


Fig. 10. 3D model of the compound motion unit.

As is shown in the Fig. 10, the compound motion equipment consists of three parts. The upper part is for the orbital movement, including the main spindle, the four-bar linkage holder, and the stroke radius adjustment. The middle part is for the sinusoidal rotation movement, including the servo motor, the transmission belt and the pulley. The lower part is for the working conditions, including the air cylinder, ball joints, and the tool base. This unit can be mounted to FSGJ series (the planer type 5-axis machine series, developed by CIOMP) through the interface.

3.2 Control

The strategy of the compound unit control is to set the main spindle (orbital motion) as an initiative movement, and set the servo motor (rotary motion) as a following movement. A schematic diagram of the control system is shown in Fig. 11. When it functions, the main spindle rotates to produce orbital movement, while a magnetic encoder reads its position. Guided by the position of the main spindle, the IMAC400 controller [22] adjusts the servo in real time, according to the feedback parameters of the following motor, to achieve closed-loop automatic control.

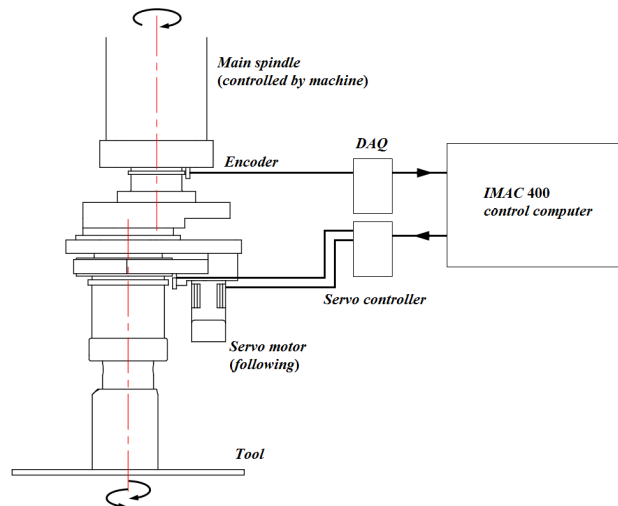


Fig. 11. Schematic diagram of the control system for the compound motion unit.

Since Eq. (4) gives the angular speed proportion of the spin and the orbital motion, the following motor can be controlled to follow in speed (ω_b) according to the position of the spindle motor (ω_a). However, considering that the servo control is based on the feedback of

the position encoder, it will facilitate the motor control, if Eq. (4) can be rewritten in the perspective of the angular position relationship,

$$\beta = k \sin \alpha + \theta_0. \quad (15)$$

Here θ_0 is the initial angle of β . The sinusoidal rotation movement is required to be consistent in phase with the orbital movement. Otherwise, any phase leads, lags, or drifts will change the orientation of the heterocercal TIF constantly or cumulatively. Besides, if the magnitude of the sinusoidal movement fluctuates, it also affects the stability and determinacy of the objective TIFs.

The PID parameters were optimized on-line, and then checked at 50Hz, $\pm 36^\circ$, which is equivalent to $\omega_a = 50$ revolutions per minute (RPM), $k = 0.1$. The maximum following error $\Delta\beta = \pm 0.022^\circ$ (0.06%). This error affects the orientation of the desired TIF no more than 0.04° . Since the spin motion is not a constant, it would impose high requirement on the servo motor, especially when the revolution speed increases. Aiming at large mirror fabrication, large tools usually run in a relatively low speed, though this application may be limited in small tools or rapid processing cases.

4. Experimental demonstration of the heterocercal TIF

Two sets of experiments were used to demonstrate the performance of the heterocercal TIFs. Figure 12(a) shows the full size of the compound motion unit as designed. But because it is difficult to get some very large workpieces for test, the size of tool was set to $\varnothing 90\text{mm}$ with a triangle tool base mounting instead of the round one, as shown in Fig. 12(b). The sizes of the SiC workpieces were around 200mm.

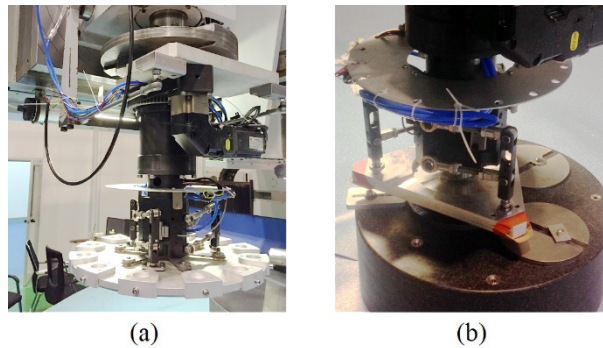


Fig. 12. Compound motion unit equipped with different sizes of tool bases. a) Normal status, equipped with a round base for $\varnothing 400\text{mm}$ tool. b) Test status, equipped with a triangle base for $\varnothing 90\text{mm}$ tool (still round tool-shape).

The working spot and the edge TIF profiles are plotted in Fig. 13 and Fig. 15. The conditions for the two TIF experiments are provided in Table 2.

Table 2. TIF experiment conditions

Experiment	No.	1	2
General	Run time	20 min	~100 min
	Polishing compound	Diamond slurry	Diamond slurry
Workpiece	Size	∅150 mm	254mm × 150mm Rect.
	Material	RB-SiC	RB-SiC
	Initial surface error	16nm RMS	13nm RMS
Tool	Polishing material	PU LP-66	PU LP-66
	Diameter	90mm	90mm
	Pressure	16.0kPa, or 2.3psi	16.0kPa, or 2.3psi
	RPM	50	49.2
	Stroke radius	9mm	9mm
	Spot size	108mm	108mm
	Swing ratio k	0.2	0.1
	Overhang ratio	None	0.208(22.5mm)
	Feeding speed ^a	0	1.658mm/min

^aFeeding direction is along the edge of work piece.

4.1 Experiment 1: single spot

The first experiment was performed using the compound motion unit to produce the heterocercal TIF. To approach the large tool conditions, the main spindle ran in a relative low revolution speed, which was 50 RPM. On the other hand, the silicon carbide (SiC) is a very hard material. Hence, the material removal rate is lower consequently. The polishing pad was made of polyurethane (PU, or PUR), and LP-66 is one of the types from Universal Photonics, Inc.

The measured spot is plotted in Fig. 13. In the central part, the heterocercal TIF has an obvious characteristic incline plane as analyzed above. In comparison to the simulated spot, the peak of the TIF is also translated as designed, without any burr, step, or distorted central V-shape. This indicates that the compound motion unit shows good performance during polishing, and the removal map agrees well with the TIF model. In Fig. 13(c), the measured profile and the simulated profile also quantitatively compared in the skewed direction, with the fitting residual less than 19nm RMS (8%). Before we utilize this equipment to converge the surface error of most area of the workpiece besides the edge, the simulated TIF can be used to predict the quality and efficiency of the coming process.

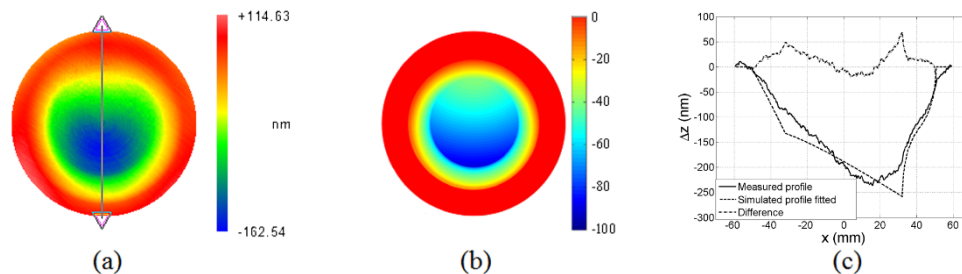


Fig. 13. The working spot of the heterocercal TIF on a ∅150mm workpiece. a) Measured spot. b) Normalized simulated spot. c) Simulative comparison.

4.2 Experiment 2: Edge TIF

In the second experiment, the workpiece was rectangular in shape, and the tool moved along the long direction hanging on the edge. The edge TIF simulation was used to set the overhang ratio to 0.208, a condition which leaves nearly no TUE residual in the simulation result. As

shown in Fig. 14, the tool path was 180mm long, and the width of the observation area was 72mm.

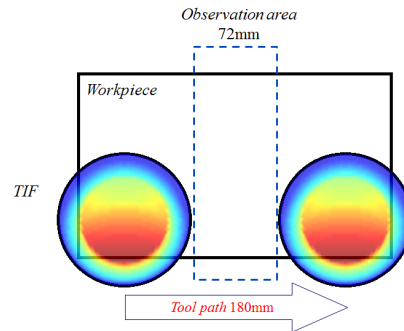


Fig. 14. Schematic diagram of the tool's movement on the workpiece.

The edge TIF was measured by ZYGO[®] interferometer, and its distribution and profile are plotted in Fig. 15 and Fig. 16 respectively. The former shows a controlled incline plane of the edge removal, with extremely small TUEs or TDEs.

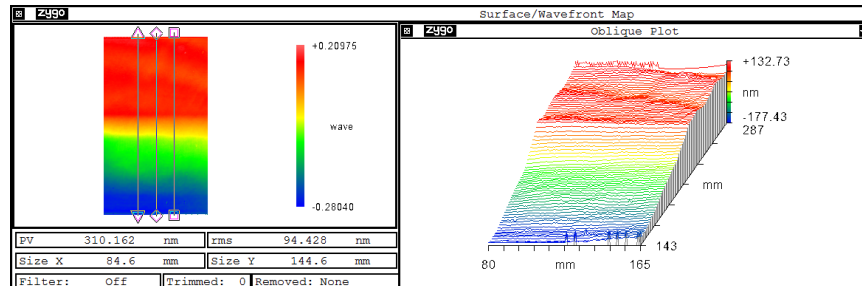


Fig. 15. Edge TIF of the heterocercal tool.

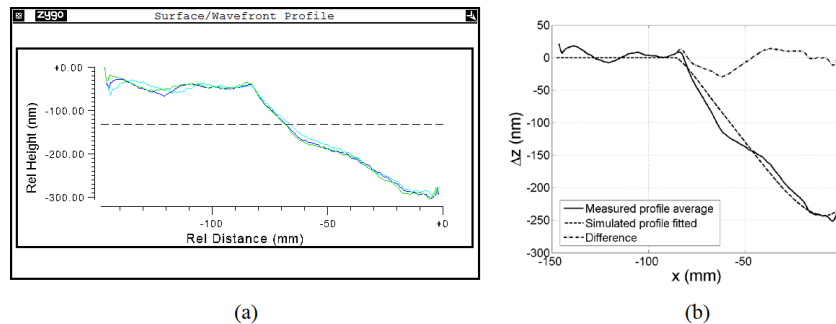


Fig. 16. Experimental result of the edge TIF profiles (a) and the simulative comparison (b).

In Fig. 16(a), three of the removal profiles (marked in Fig. 15) are plotted out, which shows a very stable removal at the edge. The peak values of the material removal were 240nm consistently. In Fig. 16(b), the measured average profile and the simulated profile were also compared, with the fitting residual less than 12nm RMS (5%), which was probably an attribute of the initial surface error (13nm RMS). Since the simulation did not involve any non-linear pressure modification at the edge, it proves that the heterocercal tool has the desired significant effect on TUEs control, and maintains the high accuracy in material removal in the overhang cases.

5. Simulation convergence of surface error map

For the task of manufacturing the future TMT M3 mirror, which is undertaken by CIOMP and not yet started, it is important to verify the convergence of surface error with our algorithm. To do this, we performed a MATLAB simulation process using the heterocercal TIF in theoretical form on a $3.5\text{m} \times 2.5\text{m}$ elliptic flat, ignoring the non-linear pressure distribution at the edge or any mechanical limitations. In this simulation, a 1.2m round tool was used to produce the orbital TIF and the heterocercal TIF respectively. The radius of stroke was set to 120mm for both operation modes. The type of tool path was double-spiral, and the pitch and pace of both operation modes were both 100mm, with maximum overhang ratio 0.20 (288mm). In the second mode, the orientation of heterocercal TIF was set along the radial direction all the time to restrain the TUEs (whenever near the edge or not), as shown in Fig. 17.

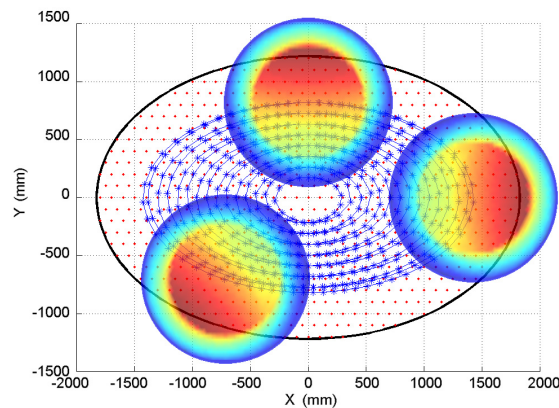


Fig. 17. Double-spiral tool path (blue dot line) and TIF orientation planning for an elliptic flat.

Simulation software for Large Aspherical Mirror (SLAM, developed by CIOMP) is used to calculate the dwell time, which calculation is based on the matrix algorithm [23]. Figure 18 shows the initial surface error map $0.67\mu\text{m}$ PV, $0.132\mu\text{m}$ RMS, and $0.38\mu\text{rad}$ slope-RMS (sampling grid size 3.4mm, hereinafter inclusive). Figure 19 and 20 show the dwell time and residual error distribution of the simulation result. In orbital mode, residual error map was $0.296\mu\text{m}$ PV, $0.056\mu\text{m}$ RMS, and $0.32\mu\text{rad}$ slope-RMS, while for heterocercal mode, it was $0.118\mu\text{m}$ PV, $0.0156\mu\text{m}$ RMS, and $0.179\mu\text{rad}$ slope-RMS. The convergence rates of RMS were 57.8% and 88.2% respectively.

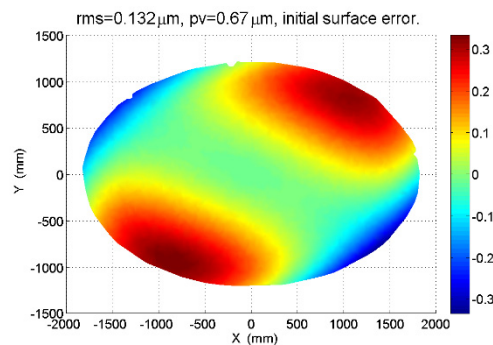


Fig. 18. Initial surface error map of $3.5\text{m} \times 2.5\text{m}$ elliptic flat (in μm).

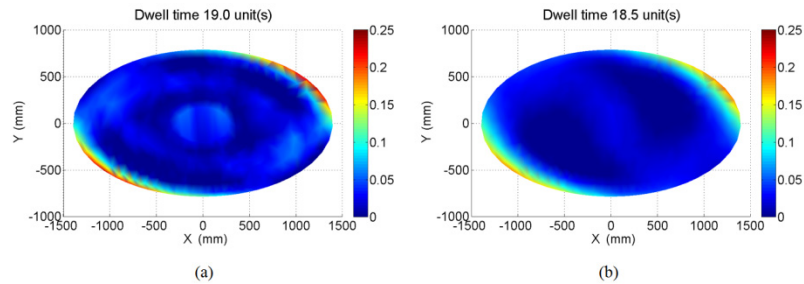


Fig. 19. Dwell time map. a) Orbital mode. b) Heterocercal mode, $k = 0.25$.

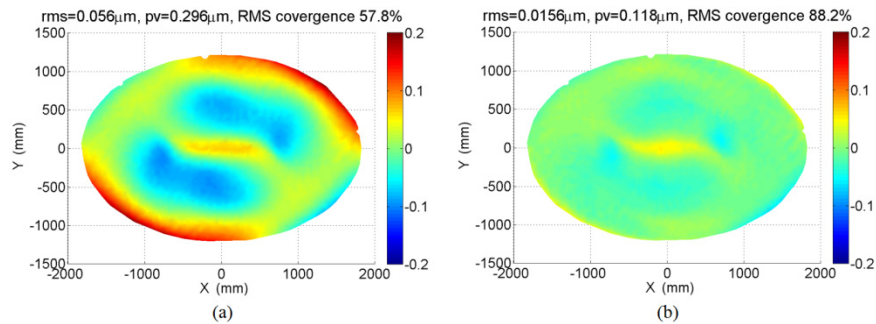


Fig. 20. Residual error map after one simulation iteration of 1.2m round tool (in μm). a) Orbital mode. b) Heterocercal mode, $k = 0.25$.

The additional swing motion did not increase any dwell time, as shown in Fig. 19, instead it effectively improves the efficiency of simulative convergence. In Fig. 20, the heterocercal mode exhibited a better performance in TUE and TDE control compared with that in orbital mode. In view of slope-RMS, the convergence rate in the heterocercal mode is even 3.4 times larger than the orbital tool.

In this simulation, the ratio of the tool diameter and the mirror size was 1:3. It also shows that the heterocercal mode is applicable for the large tool-to-mirror size ratio conditions in the CCOS process.

6. Concluding remarks

As the usage of the edge control solutions aiming at TDEs modeling is limited in some particular working conditions, we provided an idea of using a heterocercal TIF to restrain the TUEs. Previous researches on edge modeling methods did the calculations and simulations for the modified pressure distribution, while our purpose was to design and rearrange the velocity field to create a new type of TIF instead. To achieve this design, an operating mode combination of orbital motion and swing rotary motion was developed.

With the model of the new type TIF, the way that the heterocercal coefficient k changes the velocity field and the material removal distribution was analyzed. The working parameters were optimized for a better performance in TUEs control and surface error convergence. A compound motion unit was designed, physically realized, and utilized to produce the high-precision movement combining output.

Experimental demonstration for the heterocercal TIF and its edge TIF was successfully performed, which was consistent with the theoretical analysis and verified its capability in TUEs control as desired. Finally, a simulative convergence revealed the significant control to the TUEs and the entire surface errors in the large tool-to-mirror size ratio conditions. Compared to the orbital tool, the convergence rates of both RMS and slope-RMS were

increased by 50% and 240%, respectively. Improvement in convergence rate for the residual surface error is directly related to more efficient time management and lower cost for large optics fabrication projects. Its significance would be great for extremely large optical system projects.

The way we control the TUEs using the heterocercal tool is not exclusive. After all, non-linear pressure modification helps the figuring precision in most of the overhang cases. Besides, dynamic effects by introducing the tool's sinusoidal rotation may change the pressure distribution at the edge. Future work is to perform the compatibility of this new type TIF with the edge model for more accurate control of edge effects.

Funding

National Basic Research Program of China (2011CB013205); National Natural Science Foundation of China (NSFC) (61210015, 61605202).